Nanotechnology

PAPER • OPEN ACCESS

# Focused ion beam lithography for position-controlled nanowire growth

To cite this article: Aleksander B Mosberg *et al* 2023 *Nanotechnology* **34** 335301

View the article online for updates and enhancements.

You may also like

- Aluminum oxide mask fabrication by focused ion beam implantation combined with wet etching
  Zhengjun Liu, Kari Iltanen, Nikolai Chekurov et al.
- Epitaxial graphene growth on FIB patterned 3C-SiC nanostructures on Si (111): reducing milling damage
  Mojtaba Amjadipour, Jennifer MacLeod, Josh Lipton-Duffin et al.
- New insight into anodization of aluminium with focused ion beam pre-patterning
  I V Roslyakov, S E Kushnir, D M Tsymbarenko et al.

This content was downloaded from IP address 129.241.236.238 on 11/07/2024 at 09:07

OPEN ACCESS
IOP Publishing

Nanotechnology

Nanotechnology **34** (2023) 335301 (8pp)

https://doi.org/10.1088/1361-6528/acd2e1

# Focused ion beam lithography for position-controlled nanowire growth

**Aleksander B Mosberg[1,2], Dingding Ren[3], Lyubomir Ahtapodov[3], Helge Weman[3], Bjørn-Ove Fimland[3] and Antonius T J van Helvoort[1]**

[1] Department of Physics, Norwegian University of Science and Technology (NTNU), NO-7491 Trondheim, Norway
[2] SuperSTEM Laboratory, SciTech Daresbury Campus, Daresbury WA4 4AD, United Kingdom
[3] Department of Electronic Systems, Norwegian University of Science and Technology (NTNU), NO-7491 Trondheim, Norway

E-mail: a.helvoort@ntnu.no

Received 28 February 2023, revised 27 April 2023
Accepted for publication 5 May 2023
Published 1 June 2023

**Abstract**

To exploit the promising properties of semiconductor nanowires and ensure the uniformity required to achieve device integration, their position on the growth substrate must be controlled. This work demonstrates the direct patterning of a $SiO_2$/Si substrate using focused ion beam (FIB) patterning to control self-catalyzed GaAsSb nanowire growth in molecular beam epitaxy (MBE). Besides position control, FIB patterning parameters influence nanowire yield, composition and structure. Total ion dose per hole is found to be the most important parameter. Yield of single nanowires ranges from ≈34% to ≈83%, with larger holes dominated by multiple nanowires per hole. Areas exposed to low ion beam doses are selectively etched by routine pre-MBE HF cleaning, enabling patterning and nanowire nucleation with minimal damage to the Si substrate. The optical and electronic properties of nanowires are found to depend on the ion dose used during patterning, indicating the potential for FIB patterning to tune nanowire properties. These findings demonstrate the possibility for a FIB lithography protocol which could provide a rapid and direct patterning process for flexible controlled nanowire growth.

Supplementary material for this article is available online

Keywords: nanowires, FIB, patterning, GaAsSb, semiconducting nanostructures

(Some figures may appear in colour only in the online journal)

## 1. Introduction

Semiconductor nanowires are promising building blocks for next-generation electronic and optoelectronic devices with the ability to tune properties by composition, size and unique axial and/or radial hetero-structuring [1, 2]. As the lattice matching criteria are less stringent than for thin films, different III–V semiconductors can more easily be integrated with Si technology [3]. Multiple nanowire-based optoelectronic devices with promising characteristics have been demonstrated, such as solar cells [4], sensors [5], light-emitting diodes [6], single-photon sources [7] and lasers [8]. GaAsSb nanowires in particular have been shown to be a diverse III–V nanowire subgroup [9] due to their zinc-blende crystal phase purity [10, 11], intrinsic p-type doping [12–14] and tunable bandgap in the near infrared range.

The combined influence of composition, size and heterostructuring on nanowire properties means that ensuring uniformity in bottom-up nanowire growth, e.g. by molecular beam epitaxy (MBE) requires precise control of nanowire positioning and local nucleation conditions [15–19]. Especially the seeding and pinning of the liquid catalyst particle (Ga for self-catalyzed Ga-V nanowires) are crucial [20]. A

Original content from this work may be used under the terms of the Creative Commons Attribution 4.0 licence. Any further distribution of this work must maintain attribution to the author(s) and the title of the work, journal citation and DOI.

 © 2023 The Author(s). Published by IOP Publishing Ltd

common way to control this is to mask the growth substrate with a patterned oxide barrier layer [15, 21]. By creating regular patterns of holes in this oxide mask where nanowires selectively grow on the exposed substrate, ordered growth of positioned nanowires can be achieved with identical local growth conditions for each individual nanowire.

This patterned growth mask is most often created using lithography-based techniques [21–24], e.g. electron beam lithography (EBL) [15], which rely on resist patterning and etching. Alternatively, direct patterning of holes could lead to increased positioning flexibility and a simplified fabrication process. This can be achieved by a focused ion beam (FIB) [25], an approach which has so far been primarily explored in proof-of-principle studies [26–33]. These studies are mostly random area growth, but suggest that single nanowire positioning should be achievable after optimizing patterning conditions. This is explored in the present work, using fixed MBE conditions to study on a single substrate the effect of FIB milling parameters on the ranges in yield, distribution and properties of GaAsSb nanowires. The ability to position single nanowires with flexible and accurate patterning and growth initiation is a key step to enable integration of nanowires with more complex geometry such as atomic force microscopy cantilevers [27].

## 2. Experimental

In this work, a wide range of FIB-patterned mask holes is created to systematically explore the effects of different FIB patterning conditions on the nucleation and functional properties of self-catalyzed GaAsSb nanowires. Specifically, the yield, structure and optoelectronic properties are all examined and compared between different arrays of nanowires grown using a matrix of varying FIB conditions on a single substrate. This approach allows for direct comparison of different FIB-defined growth conditions, demonstrating both the viability of FIB patterning, the influence of FIB patterning on nanowire properties and the degree to which rapid FIB patterning of different hole geometries can assist in establishing optimal nanowire growth conditions. The growth substrate is a heavily p-type doped Si(111) with a 40 nm thermal grown $SiO_2$ layer. The $SiO_2$ film is patterned with a Thermo Fischer Scientific Helios Nanolab 640 Dualbeam FIB at 30 kV and 9.7 pA. FIB patterning repeatability is ensured by programming the patterning process using AutoFIB. Circular objects are defined with given depth and width.

To isolate and investigate the effect of FIB milling parameters, an $8 \times 8$ reference matrix as shown in figure 1(a) is created in the $SiO_2$ layer. This matrix combines 8 linearly increasing milling depths (from 10 to 80 nm using a standard Si application file, corresponding to an area dose of 400 to 3300 ions $nm^{-2}$) with 8 linearly increasing hole diameters (from 10 to 80 nm) to sample 64 different growth conditions, all on a single substrate to reduce potential MBE-related variation. Each growth condition contains a $15 \times 18$ array of holes with 1 $\mu$m pitch.

After FIB milling the sample is cleaned with 1% dilute HF for 150 s before insertion into a solid-source Varian GEN II Modular molecular beam epitaxy (MBE) system where it is annealed at 700 °C for 5 min. Nanowires are grown at 625 °C. After a 5 min Ga pre-deposition step with Ga flux of 0.7 monolayers per second, $As_2$ and $Sb_2$ fluxes are opened at $2.5 \times 10^{-6}$ Torr and $2 \times 10^{-7}$ Torr, respectively, for 20 min. Scanning electron microscopy (SEM) examination of the grown structures is done at 5 kV in the same Dualbeam FIB as used for patterning. Micro-photoluminescence ($\mu$-PL) studies on selected grown arrays are performed at 12 K using a closed-cycle liquid He cryostat. A laser at 532 nm is used for excitation and a single grating Andor Shamrock spectrometer with an Andor Newton line Si EMCCD camera for the PL detection. The laser was defocused to maximize signal. The spot size is approximated to 2 $\mu$m, sampling 5–7 holes near the middle of each array.

Two-point *I–V* probing is done *in situ* in a Thermo Fischer Scientific Helios NanoLab G4 FIB using Imina miBots with 100 nm and 1 $\mu$m radius W probes. The 1 $\mu$m probe is pressed against the wafer side to provide a solid back contact while the 100 nm probe is used to contact single individual nanowires through the Ga droplet. The probe in contact with the nanowire is biased while the back contact is kept at ground, thereby probing the entire nanowire including the nanowire-substrate interface. To ensure precise contact and remove the surface oxide layer, the 100 nm probe is shaped using the ion beam before being used to contact. *I–V* spectra are collected by sweeping the contacting probe with an Agilent B2900 series precision source measure unit. Further details on probing are given in supporting note 1 and supporting figure S1.

Specimen preparation for whole-nanowire transmission electron microscopy (TEM) of nanowires selected based on their *I–V* characteristics is performed in the G4 FIB system using the FIB EasyLift lift-out needle to break off specific individual nanowires which are then scraped off onto a 50 nm thick SiN film on a Si TEM grid. TEM lamellae of nanowires and their nanowire-substrate interface are prepared in the Helios NanoLab FIB using *in situ* lift-out. TEM and energy-dispersive x-ray spectroscopy (EDS) are performed in a Jeol ARM-200F operated at 200 kV and equipped with a Centurio EDS detector with 930 sr nominal solid collection angle. All EDS data analysis is performed using HyperSpy [34].

## 3. Results and discussion

Initial examination by SEM after MBE growth reveals that nanowires have grown in all arrays, shown for four arrays in figure 1(b). No nanowires have nucleated on the mask between the patterned arrays. TEM examination of representative nanowires as shown in figure 1(b), broken off and extracted using the FIB lift-out needle, reveals that their crystal structure is predominantly defect-free zinc-blende, with an anti-tapered Sb-rich core surrounded by an Sb-poor shell. More detail on this core–shell structure is given in supporting note 2. At the droplet-nanowire interface, a GaSb

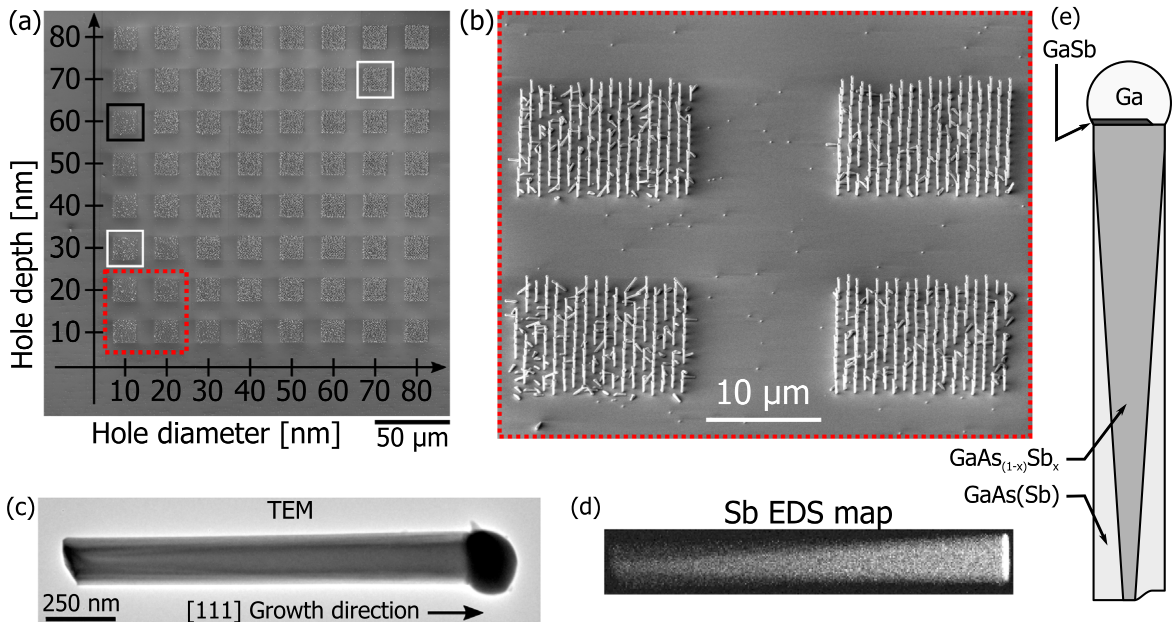


**Figure 1.** Characteristic as-grown GaAsSb nanowires. (a) 8 × 8 hole depth-diameter matrix. Arrays highlighted in white are shown in detail in figure 2, while the array highlighted in black is shown in figure 3. (b) Arrays consisting of 18 × 15 nanowires, from area marked by a red box in (a). (c) TEM of broken-off, defect-free nanowire, with (d) corresponding Sb EDS element map. (e) Schematic of representative nanowire features including GaSb crystal in Ga droplet, stepped bottom surface and anti-tapered Sb-rich core.

crystal is present (visible in figures 1(d), (e) and detailed in supporting figure S2), formed by the gradual supersaturation of Sb within the Ga droplet as the nanowire is cooled down after growth is terminated [10, 11]. Several nanowires examined feature a distinct step in the bottom surface, indicating that they have grown partly over the oxide mask.

To begin exploring the variation between different patterning conditions, two main growth regimes are identified in figure 2, primarily dependent on the total hole dose, i.e. the total number of Ga ions per patterned hole of each array: a representative example of low total hole dose arrays (hereafter referred to as low-dose), with smaller FIB-defined hole depths and diameters, is shown in (a)–(d). Low-dose arrays primarily feature a single nanowire per milled hole. In contrast, high total hole dose arrays (hereafter referred to as high-dose) with larger FIB-defined depth and diameter largely feature multiple nanowires per hole.

Examining the nanowire-substrate cross-section of a low-dose nanowire in figures 2(a)–(d), the interface is smaller than the wire itself, with the wire having nucleated on the substrate-oxide interface line (consistent with known Ga nucleation behavior [15, 35, 36]), then growing to partially cover the oxide. While ion collision cascade simulations [37] predict ion damage in the underlying Si, it appears here to be largely undamaged. This is reasonable, as MBE protocols include a 5 min annealing step at 700 °C which is known to reverse some degree of FIB-induced damage [38]. While smaller than the wire diameter, the oxide opening is still significantly larger than would be expected from FIB milling alone (figure 2(d)). The significant widening is caused by a preferential etching of ion beam exposed areas, even at doses below effective milling. More detail on this etching behavior is presented in supporting note 3 and supporting figure S3. This etching enhancement of ion beam exposed oxide when undergoing the routine HF cleaning step [32] opens the door for further low ion dose strategies. The cleaning step could be seen as an ion beam lithography developing step [39], providing a rapid and flexible technique for ion beam-patterned nanowire growth while reducing the impact of Ga implantation and amorphization.

Examining a similar high-dose cross-section in figures 2(e)–(i), multiple nanowires are present for each hole, often accompanied by parasitic growth. At these doses the hole milled into the Si substrate is significant, and it is again clear that etching significantly widens the oxide opening. Unlike the low-dose regime, the annealing step has not been able to reverse the FIB-induced effects and there is visible damage to the Si crystal structure directly under the milled hole in figure 2(f). The hole itself is largely filled with parasitic growth, while the vertical nanowire (to the right) is centered 170 nm away from the hole, making contact with the substrate-oxide interface line. Unlike the low-dose regime, here the whole nanowire is in full contact with the Si substrate as observed in figures 2(g), (i). Closer observation of the array in figure 2(e) reveals that nucleation of multiple nanowires is the case for most holes, with nanowires distributed around the perimeter of the hole in the oxide mask. This is consistent with known Ga nucleation behavior, as excessively rough surfaces and high aspect ratio holes are less suitable for nanowire growth [40, 41].

To demonstrate the transition between the low-dose and high-dose growth regimes across the 8 × 8 matrix, SEM and computer vision (CV) are combined in figure 3 to provide a quantitative and representative characterization of every nanowire from every array [42]. Unlike tilted-view SEM images as shown in figure 3(a), top-down SEM images

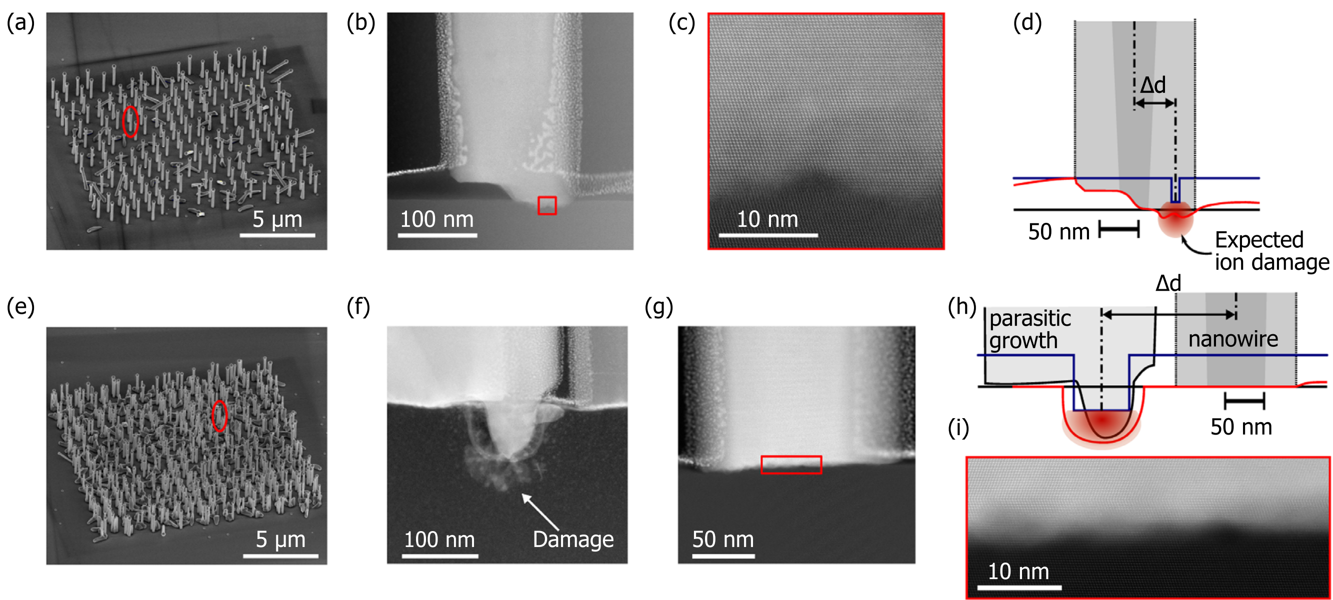


**Figure 2.** Ion-beam dependent nanowire-substrate interfaces for different milling parameters. TEM lamella specimens taken from the fields marked by white squares in figure 1(a) (bottom-left and top-right in the 8 × 8 growth matrix): (a)–(d) SEM, HAADF-STEM and schematic of nanowire from representative low-dose array. (e)–(i) SEM, HAADF-STEM and schematic from representative high-dose array. Nanowires in (b) and (g) are marked with red circles in (a) and (e), respectively. High-resolution HAADF-STEM of their interfaces at the marked red rectangles is presented in (c) and (i). In the schematic presentations (d) and (h), the solid horizontal dark blue line marks the location and shape of FIB milling while the red line marks the final observed interface after HF etching, annealing and nanowire growth. Red areas mark the expected extent of ion implantation from simulation. The distance $\Delta d$ between dash-dot lines denote the nanowire displacement (distance between targeted hole center and nanowire center axes).

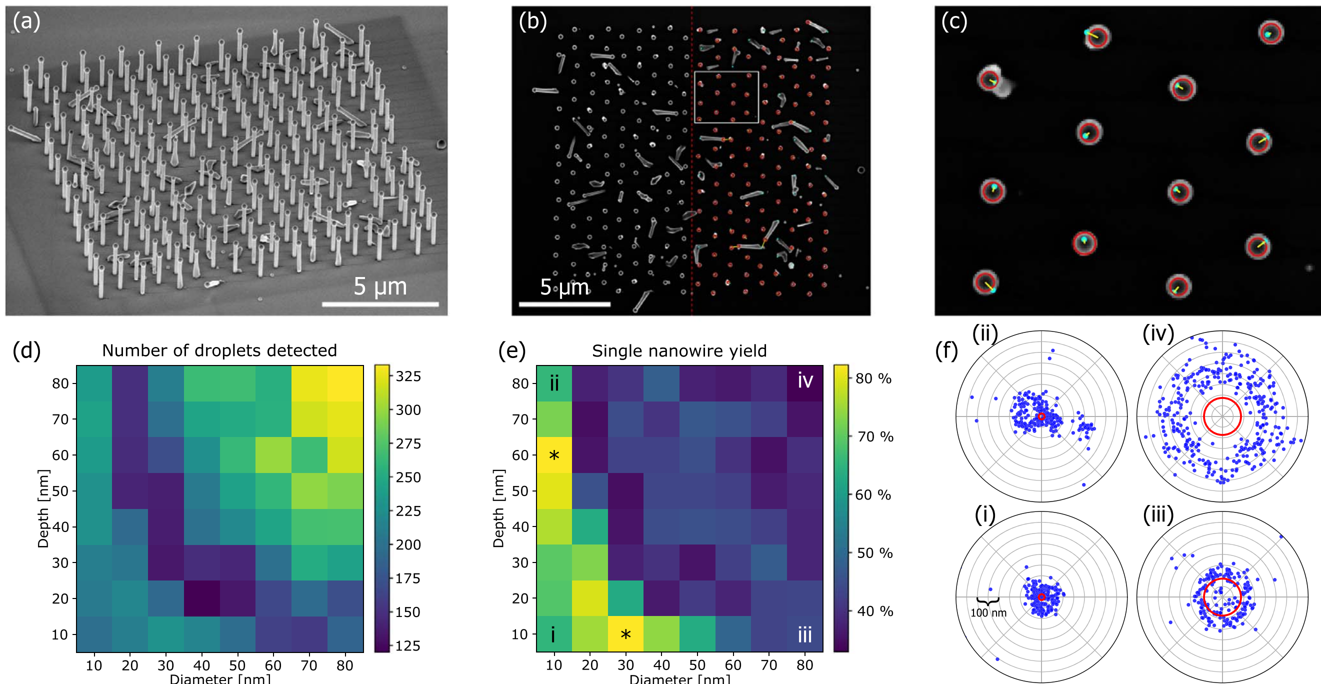


**Figure 3.** SEM-based computer vision for analysis of nanowire growth statistics: (a) tilted-view SEM image of nanowire array (depth 60 nm, diameter 10 nm) highlighted in black in figure 1(a). (b) Top-down SEM image of same array, optimized for computer vision with detected droplets in red (right half). (c) Enlarged image from highlight in (b) with Ga nanowire droplets, fitted hole position (cyan dots) and calculated position displacement ($\Delta d$, yellow lines). (d) 8 × 8 representation of the milled matrix with total number of detected droplets for each array in figure 1(a), each array having 270 hole positions. (e) Single nanowire yield, plotting the percentage of holes from each array with a single Ga nanowire droplet detected. Fields marked with * have yield of ≈83%. (f) Scatter plot of droplet positions relative to FIB-milled hole position from each of the four arrays indicated with (i)–(iv) in (e). Red circles indicate the input FIB patterning diameter.

(figure 3(b)) provide strong contrast from Ga droplets on top of nanowires. These droplets can then be recognized by CV, as shown in figures 3(b)–(c). By comparing the number, size and location of each detected droplet to the known as-milled pattern, each array can be characterized quantitatively. The total number of nanowires detected per array is presented in figure 3(d), demonstrating a general trend across the FIB depth-diameter parameter space: as holes increase in both depth and width, nanowire yield first goes down due to parasitic growth, but then recovers and increases further as holes start to nucleate multiple nanowires per hole. Given the occurrence of multiple nanowires per hole, direct counting of nanowires would result in yield values above 100%. To account for this, single nanowire yield is determined by comparing the positions of all nanowires to the known pattern of FIB-milled holes. Each hole can be assigned one or multiple nanowires, and the percentage of holes where a single nanowire has grown can be determined. As demonstrated in figure 3(e), yield of single nanowires ranges between ≈31% and ≈83%, with the maximum achieved at two different depth-diameter combinations (marked (*) in figure 3(e)). The tendency demonstrated in figure 2 of nanowires to nucleate along the edge of holes can now also be examined in more detail. The position of each individual nanowire compared to its fitted hole location can be plotted per array, shown for the four matrix corners in figure 3(f). Plots for all 64 arrays are given in supporting figure S4. Notably, for the high-dose regime, nanowires form rings around the hole, with no Ga nanowire droplet detected over the hole itself, clearly demonstrating the impact of milling conditions on nanowire positioning uniformity with subsequent effects on the uniformity in final nanowire properties. This tendency of nanowires to nucleate along the substrate-interface line has been documented for other patterning methods [15, 21]. The FIB patterning itself is found to be uniform and unaffected by e.g. charging or drift, see supporting figure S5. As increasing ion dose leads to prominent hole milling into the substrate, nanowires nucleate on the exposed and relatively flat (though still textured) substrate around the hole.

To examine the impact of FIB milling parameters on optical properties, low-temperature (12 K) $\mu$-PL measurements are carried out with a defocused laser spot centered on each array. Plotting the PL emission peak energy for different arrays (figure 4(a)), a consistent shift in PL peak energy can be observed across the matrix in figure 4(b). Small variations in peak width and shape are ascribed to each spectrum sampling 5–7 holes with potentially varying composition or different growth, such as inclined nanowires or parasitic growth. These can be seen in SEM images, for example figure 3(a). The PL peak energy is found to have an inverse correlation with total dose, going from 1.30 eV for the smallest holes (bottom left) to 1.24 eV for the largest holes (top right). This shift in peak energy is attributed primarily to increasing Sb [43] content in the GaAsSb nanowires, increasing from around 5.4 at% to around 7 at% with increasing hole size. The rate of change for the PL peak energies over the matrix is shown in figure 4(c) to be linearly increasing with the exponentially increasing total ion dose per hole.

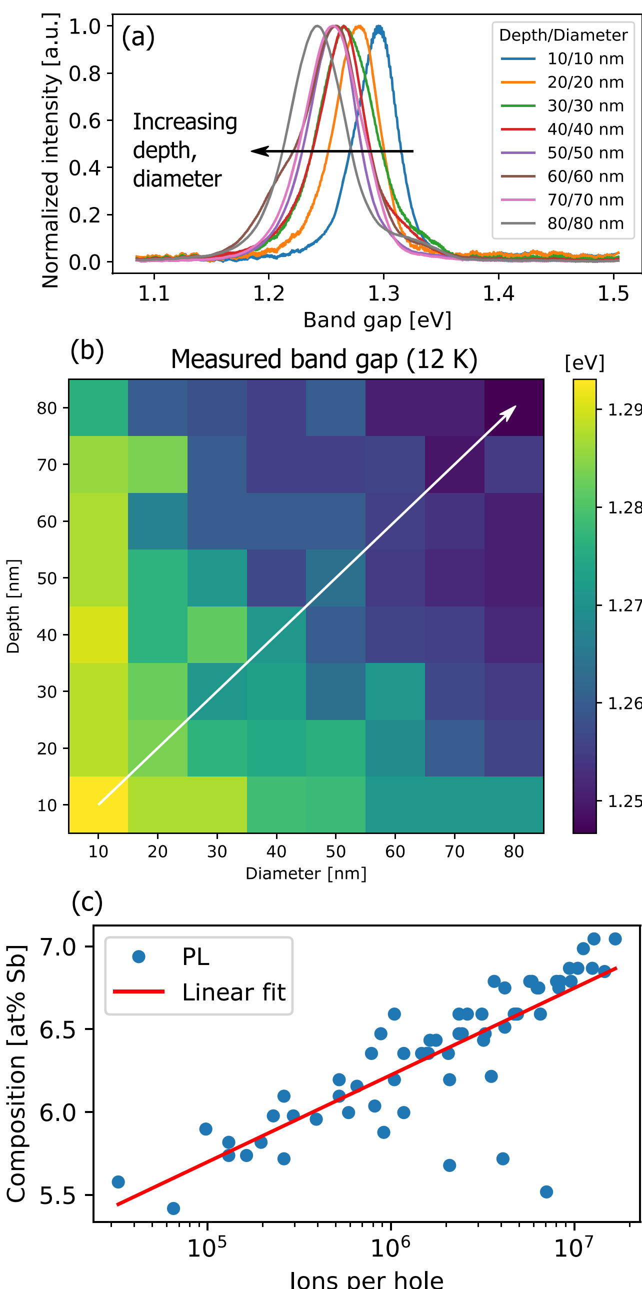


**Figure 4.** Low temperature (12 K) $\mu$-PL. (a) Representative PL spectra for the arrays along the line marked in (b) by a white arrow. (b) GaAsSb nanowire band gap as measured by PL for each array. (c) Sb content in at% in the Sb-rich core (as determined from the PL peak energy) for each nanowire array plotted against total hole dose.

This shift in the GaAsSb nanowire band gap can be compared with the change in total nanowire yield from CV. As larger areas of Si are exposed per hole, both parasitic growth and multiple nanowires per hole become more common with the net effect of turning growth from a diffusion-limited regime to a more competitive regime. This regime transition has been previously observed in GaAsSb nanowires by decreasing the patterning pitch [44], resulting in increased Ga competition which reduces droplet size. As smaller droplets incorporate less As, the Sb content increased resulting in

a redshift in PL emission peak energy, in agreement with the shift observed in figure 4(c).

As seen in figures 2 and 4, both the characteristics of the nanowire-substrate interface and the composition of the grown nanowires exhibit consistent changes across the FIB milling conditions used. It is thus to be expected that the electronic properties of the wires are also altered as a function of applied ion dose. To examine possible trends due to FIB milling conditions, a two-point probing setup within the FIB is used on as-grown nanowires across several arrays. By probing a substantial number of single nanowires, a comparison can also be made between wire-to-wire variations for each condition, and any consistent trends due to FIB milling conditions. An *in situ* sharpened W probe serves as top contact (figure 5(a)), with a second probe as back contact on the Si substrate. This enables relatively easy probing of a large number of nanowires. In total, more than 200 different nanowires were probed as-grown for this analysis. The *I–V* response of a majority of nanowires is dominated by diode behavior, shown for a range of representative nanowires in figure 5(b). While there can be significant wire-to-wire variations within each array, even from morphologically identical nanowires, two general observations are clear when comparing distributions across the matrix. First, higher doses lead to a markedly improved conductance for the probed voltage range. To quantify this, the *I–V* spectra are fitted with a two-segment piecewise linear model. From this model the estimated threshold voltage can be plotted for each probed nanowire. Figure 5(c) depicts the threshold voltage distributions for 150 nanowires from 10 different arrays, demonstrating the trend with increasing ion dose per hole. The details of this quantification are presented in supporting figure S1. Second, for larger holes such as presented in figures 2(e)–(i) the reverse current for some nanowires becomes more pronounced. The general *I–V* spectra for these nanowires resemble less a single diode and more closely the metal-semiconductor-metal behavior observed in doped GaAs nanowires [45, 46]. This demonstrates that the *I–V* characteristics of individual nanowires, like the composition and growth statistics, can be controlled by FIB milling conditions.

## 4. Conclusions

FIB milling is used to directly pattern a two-dimensional matrix of FIB patterning parameters on a single substrate. The resulting nanowires are characterized using SEM-based CV, *in situ I–V* probing on a large number of wires, *ex situ* PL and TEM. In all, the different characterizations presented demonstrate the robustness and general impact of FIB milling conditions on GaAsSb nanowire growth. While for some characteristics such as the radial distribution of nanowires in their holes, different effects of FIB-milled width and depth can be distinguished, the main trends depend largely on the total number of ions per hole. As ion dose increases, single nanowire yield increases to a maximum of ≈83% before

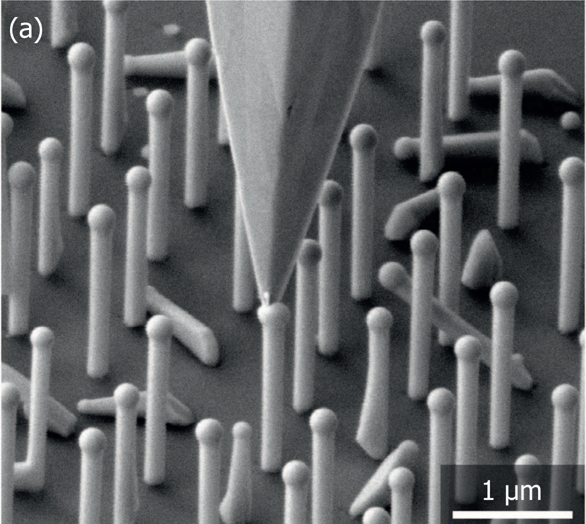


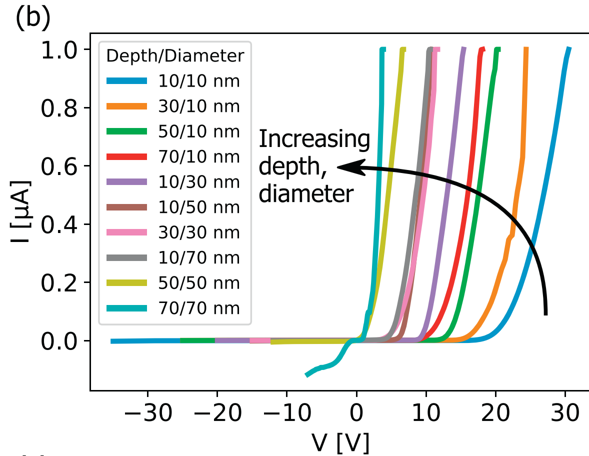


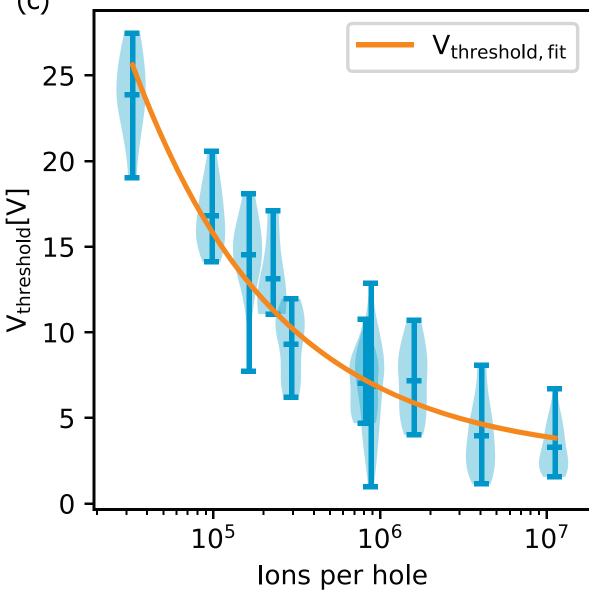


**Figure 5.** *I–V* measurements on different arrays. (a) SEM image of single nanowire probing. (b) Single nanowire *I–V* curves from the 10 arrays probed with general trend. Positive voltage bias is here defined with current flowing in the growth direction of the nanowire. (c) Violin plot demonstrating trend in threshold voltage with increasing total hole dose.

decreasing due to parasitic growth and gradual domination of multiple nanowires per hole. Patterning with a higher dose is accompanied by a reduction in band gap due to increased Sb content, higher conductance and more pronounced metal-semiconductor-metal *I–V* behavior. At lower total hole doses, FIB-related ion damage is largely recovered by standard pre-growth high-temperature treatments. The ability of Ga to enhance the etching in the HF cleaning step is demonstrated. For low doses, sites for nanowire growth are thereby created through what is effectively a FIB lithography process. Overall, FIB can be a flexible approach for direct patterning to achieve position-controlled and tunable nanowire growth.

## Acknowledgments

The authors acknowledge NTNU ford support through the Enabling technologies: NTNU Nano program. The Research Council of Norway is acknowledged for support through the Norwegian Center for Transmission Electron Microscopy: NORTEM (Grant No. 197405), the Norwegian Micro- and Nano-Fabrication Facility: NorFab (Grant No. 245963) and the NANO2021 program (Grant No. 239206). SuperSTEM is the UK National Research Facility for Advanced Electron Microscopy, supported by the Engineering and Physical Sciences Research Council (EPSRC) through grant reference EP/W021080/1.

## Data availability statement

All data that support the findings of this study are included within the article (and any supplementary files).

## Supporting materials

Supporting data includes notes on the data processing of *I–V* data, the GaAs-GaAsSb core–shell structure and the preferential HF etching of Ga exposed oxide. Details of the *I–V* processing procedure, lattice images and element composition maps of the GaSb crystal, evidence of preferential HF etching, nanowire $\Delta d$ scatter plots for all arrays and a FIB patterning uniformity analysis are included as supporting figures.

## ORCID iDs

Aleksander B Mosberg https://orcid.org/0000-0002-1575-4804
Dingding Ren https://orcid.org/0000-0001-6829-6475
Helge Weman https://orcid.org/0000-0001-5470-9953
Bjørn-Ove Fimland https://orcid.org/0000-0002-0210-4351
Antonius T J van Helvoort https://orcid.org/0000-0001-6437-1474

## References

[1] Joyce H J *et al* 2011 *Prog. Quantum Electron.* **35** 23–75
[2] McIntyre P C and Fontcuberta i Morral A 2020 *Mater. Today Nano* **9** 100058
[3] Kavanagh K L 2010 *Semicond. Sci. Technol.* **25** 024006
[4] Wallentin J *et al* 2013 *Science* **339** 1057–60
[5] Soci C, Zhang A, Bao X Y, Kim H, Lo Y and Wang D 2010 *J. Nanosci. Nanotechnol.* **10** 1430–49
[6] Tomioka K, Motohisa J, Hara S, Hiruma K and Fukui T 2010 *Nano Lett.* **10** 1639–44
[7] Reimer M E, Bulgarini G, Akopian N, Hocevar M, Bavinck M B, Verheijen M A, Bakkers E P A M, Kouwenhoven L P and Zwiller V 2012 *Nat. Commun.* **3** 737
[8] Ren D, Ahtapodov L, Nilsen J S, Yang J, Gustafsson A, Huh J, Conibeer G J, van Helvoort A T, Fimland B O and Weman H 2018 *Nano Lett.* **18** 2304–10
[9] Ren D, Ahtapodov L, van Helvoort A T J, Weman H and Fimland B O 2019 *Nanotechnology* **30** 294001
[10] Conesa-Boj S, Kriegner D, Han X L, Plissard S, Wallart X, Stangl J, Fontcuberta i Morral A and Caroff P 2014 *Nano Lett.* **14** 326–32
[11] Ren D *et al* 2016 *Nano Lett.* **16** 1201–9
[12] Huh J, Yun H, Kim D C, Munshi A M, Dheeraj D L, Kauko H, van Helvoort A T J, Lee S, Fimland B O and Weman H 2015 *Nano Lett.* **15** 3709–15
[13] Li L *et al* 2017 *Nano Lett.* **17** 622–30
[14] Wang X, Pan D, Han Y, Sun M, Zhao J and Chen Q 2019 *ACS Appl. Mater. Interfaces* **11** 38973–81
[15] Plissard S, Larrieu G, Wallart X and Caroff P 2011 *Nanotechnology* **22** 275602
[16] Munshi A M, Dheeraj D L, Fauske V T, Kim D C, van Helvoort A T J, Fimland B O and Weman H 2012 *Nano Lett.* **12** 4570–6
[17] Zhang Y, Wu J, Aagesen M, Holm J, Hatch S, Tang M, Huo S and Liu H 2014 *Nano Lett.* **14** 4542–7
[18] Yuan X, Caroff P, Wong-Leung J, Tan H H and Jagadish C 2015 *Nanoscale* **7** 4995–5003
[19] Vukajlovic-Plestina J, Kim W, Dubrovski V G, Tütüncüoğlu G, Lagier M, Potts H, Friedl M and Fontcuberta i Morral A 2017 *Nano Lett.* **17** 4101–8
[20] Matteini F, Tütüncüoglu G, Potts H, Jabeen F and Fontcuberta i Morral A 2015 *Cryst. Growth Des.* **15** 3105–9
[21] Munshi A M *et al* 2014 *Nano Lett.* **14** 960–6
[22] Plissard S, Dick K A, Larrieu G, Godey S, Addad A, Wallart X and Caroff P 2010 *Nanotechnology* **21** 385602
[23] Gibson S J, Boulanger J P and LaPierre R R 2013 *Semicond. Sci. Technol.* **28** 105025
[24] Coulon P M *et al* 2019 *Microsyst. Nanoeng.* **5** 1–12
[25] Volkert C A and Minor A M 2007 *MRS Bull.* **32** 389–99
[26] Jun K and Jacobson J M 2010 *Nano Lett.* **10** 2777–82
[27] Jenke M G, Lerose D, Niederberger C, Michler J, Christiansen S and Utke I 2011 *Nano Lett.* **11** 4213–7
[28] Diao K, Zhang J, Zhou M, Tang Y, Wang S and Cui X 2014 *Appl. Surf. Sci.* **317** 220–5
[29] Detz H, Kriz M, Lancaster S, MacFarland D, Schinnerl M, Zederbauer T, Andrews A M, Schrenk W and Strasser G 2017 *J. Vac. Sci.Technol.* B **35** 011803
[30] Lancaster S, Kriz M, Schinnerl M, MacFarland D, Zederbauer T, Andrews A M, Schrenk W, Strasser G and Detz H 2017 *Microelectron. Eng.* **177** 93–7
[31] Scholz S, Schott R, Labud P A, Somsen C, Reuter D, Ludwig A and Wieck A D 2017 *J. Cryst. Growth* **470** 46–50
[32] Bahrami D, Kashani S M M, Hassan A A, Davtyan A and Pietsch U 2020 *Nanotechnology* **31** 185302

[33] Shandyba N, Balakirev S, Sharov V, Chernenko N, Kirichenko D and Solodovnik M 2023 *Int. J. Mol. Sci.* **24** 224
[34] de la PeñaF *et al* (2018) Hyperspy/hyperspy v1.4.1 Zenodo (https://doi.org/10.5281/zenodo.1469364)
[35] Gibson S and LaPierre R 2013 *Phys. Status Solidi (RRL)* **7** 845–9
[36] Vukajlovic-Plestina J *et al* 2019 *Nat. Commun.* **10** 1–7
[37] Ziegler J F, Ziegler M D and Biersack J P 2010 *Nucl. Instrum. Methods Phys. Res.* B **268** 1818–23
[38] Xiao Y J, Fang F Z, Xu Z W, Wu W and Shen X C 2013 *Nucl. Instrum. Methods Phys. Res.* B **307** 253–6
[39] Gamo K 1996 *Microelectron. Eng.* **32** 159–71
[40] Jacobsson D, Panciera F, Tersoff J, Reuter M C, Lehmann S, Hofmann S, Dick K A and Ross F M 2016 *Nature* **531** 317–22
[41] Harmand J C, Patriarche G, Glas F, Panciera F, Florea I, Maurice J L, Travers L and Ollivier Y 2018 *Phys. Rev. Lett.* **121** 5
[42] Mosberg A B, Myklebost S, Ren D, Weman H, Fimland B O and van Helvoort A T J 2017 *J. Phys.: Conf. Ser.* **902** 012020
[43] Teissier R, Sicault D, Harmand J C, Ungaro G, Le Roux G and Largeau L 2001 *J. Appl. Phys.* **89** 5473–7
[44] Ren D, Huh J, Dheeraj D L, Weman H and Fimland B O 2016 *Appl. Phys. Lett.* **109** 243102
[45] Fauske V T, Kim D C, Munshi A M, Dheeraj D L, Fimland B O, Weman H and van Helvoort A T J 2014 *J. Phys.: Conf. Ser.* **522** 012080
[46] Fauske V, Erlbeck M, Huh J, Kim D, Munshi A, Dheeraj D, Weman H, Fimland B and Van Helvoort A 2016 *J. Microsc.* **262** 183–8